ACS APPLIED MATERIALS & INTERFACES

www.acsami.org
Research Article

First-Principles Study on the Interplay of Strain and State-of-Charge with Li-Ion Diffusion in the Battery Cathode Material $LiCoO_2$

Zizhen Zhou,* Claudio Cazorla, Bo Gao, Huu Duc Luong, Toshiyuki Momma, and Yoshitaka Tateyama*

Cite This: *ACS Appl. Mater. Interfaces* 2023, 15, 53614−53622
Read Online
ACCESS | Metrics & More | Article Recommendations | Supporting Information

ABSTRACT: Cathode degradation of Li-ion batteries (Li^+) continues to be a crucial issue for higher energy density. A main cause of this degradation is strain due to stress induced by structural changes according to the state-of-charge (SOC). Moreover, in solid-state batteries, a mismatch between incompatible cathode/electrolyte interfaces also generates a strain effect. In this respect, understanding the effects of the mechanical/elastic phenomena associated with SOC on the cathode performance, such as voltage and Li^+ diffusion, is essential. In this work, we focused on $LiCoO_2$ (LCO), a representative LIB cathode material, and investigated the effects of biaxial strain and hydrostatic pressure on its layered structure and Li^+ transport properties through first-principles calculations. With the nudged elastic band technique and molecular dynamics, we demonstrated that in Li-deficient LCO, compressive biaxial strain increases the Li^+ diffusivity, whereas tensile biaxial strain and hydrostatic pressure tend to suppress it. Structural parameter analysis revealed the key correlation of "Co layer distances" with Li^+ diffusion instead of "Li layer distances", as ordinarily expected. Structural analysis further revealed the interplay between the Li−Li Coulomb interaction, SOC, and Li^+ diffusion in LCO. The activation volume of LCO under hydrostatic pressure was reported for the first time. Moreover, vacancy formation energy calculations showed that the Li intercalation potential could be decreased under compressive biaxial strain due to the weakening of the Li−O bond interaction. The present findings may serve to improve the control of the energy density performance of layered cathode materials.

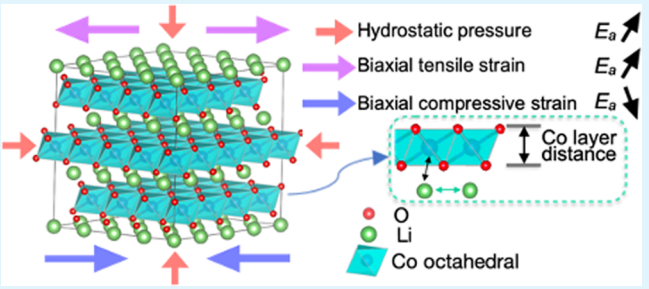

KEYWORDS: *biaxial strain, hydrostatic pressure, layered cathode material, ionic diffusion, vacancy*

1. INTRODUCTION

Rechargeable Li^+ batteries (LIBs) not only power most of today's portable electronic devices but have also led to a revolution in electric vehicles. Such strong market incentives demand higher energy storage capabilities and power characteristics of LIBs. The main focus lies on cathodes, which have the determining role in defining LIB properties.[1−3] Meanwhile, structural degradation, which results in capacity and voltage fading, is one of the main problems affecting the performance of cathodes. Because Li^+ is rapidly extracted and inserted in cathodes during the charging and discharging processes, the lattice parameters of the crystalline structure rapidly change. This charge/discharge cycle induces stresses and strains that can potentially cause microcracking.[4,5] For example, Tan et al.[6] observed the crystal damage in the $LiNi_{0.9}Co_{0.05}Mn_{0.05}O_2$ (NCM) cathode during the charging process. By using *in situ* XRD characterization, they observed internal strain and stress accumulation upon Li^+ extraction.

Apart from stress inside the cathode structures, strain phenomena also happen at the interface between cathodes and solid electrolytes due to the interface lattice mismatch.[7−9] Previous works discussed how such strain could weaken the interface interaction and eventually retard the battery performance.[10,11] As the focus shifts toward the development of all-solid-state LIBs, the application of external pressure becomes crucial to enhance the contact area between the Li electrode and solid electrolyte, ensuring smooth battery operations. This pressure typically ranges from dozens to hundreds of MPa or even several GPa.[12,13]

On the other hand, previous research has demonstrated that Li^+ diffusion can be greatly enhanced in solid-electrolyte and anode materials under external biaxial strain.[14−16] This manipulation of the lattice via strain effects raises fundamental scientific questions because it is an effective way of modulating ionic conductivity in oxide materials. Regarding the effects of strain on Li^+ cathode materials, $LiFePO_4$ has been studied via various simulation methods. Lee et al.[16] performed density

Received: September 27, 2023
Revised: October 20, 2023
Accepted: October 24, 2023
Published: November 9, 2023

functional theory (DFT) calculations and predicted that a 4% biaxial tensile strain would increase the room-temperature electronic and Li^+ ion conductivities 15- and 50-fold, respectively. Similarly, Tealdi et al.[17] conducted classical molecular dynamics (MD) simulations to investigate the strain effects on the ion conduction and defect formation in olivine Li^+- and Na^+-based cathode materials. They predicted a sudden drop in the activation energy of Li^+ diffusion at room temperature for tensile strain applied within a certain plane, leading to a significant enhancement in the ionic conductivity. For the investigation of such strain and stress effects, theoretical simulation has been regarded as an effective tool that allows us to understand the strain and stress mechanisms at the atomistic level.[18]

$LiCoO_2$ (LCO), as a representative cathode material that has been commercialized for nearly 30 years, still shows great potential for further enhancement of its energy density.[19] Even though it is one of the most prominent layered intercalated Li^+ cathode materials, LCO was reported to display complicated internal strain and stress patterns generated during charging/discharging processes.[20−22] Additionally, the effect of hydrostatic pressure—which inevitably arises during the assembly of battery components—remains poorly understood. As such, an understanding of the strain and stress effects on Li^+ diffusion under different charging states is still lacking.

In this article, we aim to investigate the impact of external biaxial strain and hydrostatic pressure on the Li^+ diffusion behavior of LCO with varying state-of-charge (SOC) by means of first-principles calculations based on density functional theory (DFT). We hope that the present work will advance knowledge of the complex role played by strain and stress effects in LCO during charge/discharge cycles as well as in other similar layered materials employed as battery cathodes.

2. COMPUTATIONAL METHODS

First-principles calculations based on DFT were carried out using the generalized gradient approximation of Perdew−Burke−Ernzerhof (GGA-PBE) as it is implemented in the Vienna *Ab initio* Simulation Package (VASP) software.[23] The projector-augmented wave method (PAW) was employed to represent the ionic cores by considering the following electronic states as valence: Li 1*s*, 2*s*, and 2*p*; Co 4*s* and 3*p*; and O 2*s* and 2*p*.[24] A "Hubbard-*U*" scheme was used to correct the localized electronic states of Co. In this paper, the *U* value used for Co is 4.91 eV.[25] In terms of bulk structures, the LCO unit cell ($R\bar{3}m$ space group) was fully optimized and relaxed until the total energies were converged to within 1 meV/atom and the forces in the atoms were all below 0.01 eV/Å by using an energy cutoff of 650 eV and a Monkhorst−Pack k-point grid of 10 × 10 × 2. The relaxed LCO unit cell lattice had the parameters $a = b = 2.83$ Å and $c = 14.15$ Å, which are in good agreement with previous theoretical and experimental studies.[26−28]

Biaxial strain is defined as $\eta = (a - a_0)/a_0$, where a_0 represents the equilibrium in-plane lattice parameter (shown in Figure 1 a,b). A positive η is regarded as tensile biaxial strain, whereas a negative η is regarded as compressive. Energy-minimized structures were subjected to biaxial strains ranging from −4% (compressive) to +4% (tensile) in the *a, b* plane while the out-of-plane lattice parameter *c* was fully relaxed. The range of biaxial strains applied in our study was determined based on the findings of a recent experimental investigation by Zhu et al., where they observed ∼4% residual strain aligned parallel to the LCO < 003> plane.[29] The same strain range was also observed and discussed in a recent study by Wang et al.[30] These strained energy-minimized structures were used as the initial configurations in subsequent electronic structure and ion migration calculations. Similar methodologies were reported in previous studies of Li^+ cathode and solid oxide fuel cell materials.[17,31]

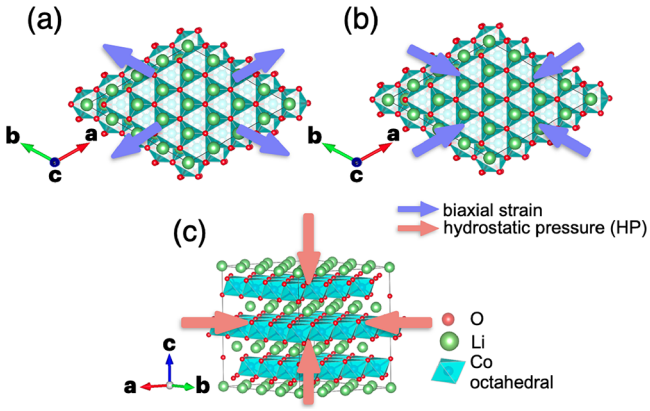

Figure 1. Schematic view of external (a) biaxial tensile strain, (b) biaxial compressive strain, and (c) hydrostatic pressure (HP) applied to $LiCoO_2$.

In terms of the hydrostatic pressure (HP), shown in Figure 1c, around 1 GPa was exerted on the energy-minimized structures, which were subsequently reoptimized and employed in further calculations. We simulated biaxial stress on the *a, b* plane by simultaneously applying strain in both lattice vectors and HP by applying a pressure of ∼1 GPa along the three axes. The stress induced is shown in Figure S1. The strain along the *a* and *c* axes as a function of biaxial strain can be found in Figure S2.

Nudged-elastic band (NEB) calculations were conducted to estimate the Li^+ migration pathway and activation energy barrier (E_a) within the vacancy-mediation regime.[32] An energy cutoff of 520 eV and a simulation cell containing 192 atoms ($Li_{48}Co_{48}O_{96}$) before vacancy creation were used. Two pathways, with one and two Li vacancies (where Li vacancy concentrations are 0.98 and 0.96), respectively, were examined.

First-principles molecular dynamics (FPMD) simulations based on DFT were performed in the canonical (*N, V, T*) ensemble with a time step of 1 fs. In a trade-off between the computational cost and accuracy, only the Γ-point grid for Brillouin zone sampling and an energy cutoff of 400 eV were set for all FPMD calculations. The selected volumes and geometries were those determined at zero-temperature conditions; hence, we neglected thermal expansion effects. The temperature in the FPMD simulations kept fluctuating around a preset value by employing the Nosé−Hoover thermostat. The calculations comprised a total simulation time of ∼100 ps. We performed three FPMD simulations for each of T = 800, 1000, 1200, and 1400 K, considering an η of −4, 0, and +4%. All configurations were visualized using the VESTA software.[33] Additional FPMD calculations for energy cutoffs of 600 and 800 eV were performed for 20 ps at 1200 K to obtain the average stress tensors. We compared the results to those obtained with an energy cutoff of 400 eV and found that the average stress tensors (*xx*, *yy*, and *zz*) calculated with the lower cutoff vary within ±2%, indicating the plausibility of using 400 eV as the cutoff energy for the following FPMD calculation. The Li^+ ionic diffusion coefficient (D^*) is estimated based on the mean squared displacement (MSD) using the following formula:

$$D^* = \frac{1}{2Ndt}\sum_{i=1}^{N}\langle[r_i(t+t_0) - r_i(t_0)]^2\rangle \quad (1)$$

where N and d indicate the number of Li^+ included and the dimensionality in the system, respectively. t_0 and $r_i(t)$ refer to the initial time and the displacement of the *i*th Li^+ at time *t*. The activation energy (E_a) was assumed to follow the Arrhenius equation:

$$D^*(T) = D_0 \times \exp\left(-\frac{E_a}{k_B T}\right) \quad (2)$$

where D_0 is the pre-exponential factor and k_B is the Boltzmann constant. E_a and D_0 are adopted by the extrapolation from the

https://doi.org/10.1021/acsami.3c14444
ACS Appl. Mater. Interfaces 2023, 15, 53614−53622

temperatures FPMD was performed at to room temperature (300 K) because of the poor Li^+ diffusion of LCO at lower temperatures. Such a strategy has been employed in previous simulation works for solid electrolytes.[34,35]

Ionic conductivities were obtained with the Nernst−Einstein relationship:

$$\sigma(T) = \frac{Ce^2}{k_B T} D^*(T) \quad (3)$$

where C and e are the concentration and charge of Li^+ ions. For the calculation of vacancy formation energies, E_V, we removed one Li from the simulation supercell.

All point defects were assumed to be neutrally charged, and E_V was computed using the following formula:

$$E_V = E_{defect} - E_{perfect} + \mu_i \quad (4)$$

where E_{defect} is the total energy of the system containing the Li vacancy, $E_{perfect}$ is the total energy of the system without any defect, and μ_i is the chemical potential of Li metal, which was estimated from the formation energy of bulk bcc Li metal as equal to −1.904 eV.

3. RESULTS AND DISCUSSION

3.1. Zero-Temperature Activation Energy for Li^+ Diffusion under Biaxial Strain. The NEB method was used to calculate the migration energy barrier (E_a) as a function of the biaxial strain. Two possible diffusion pathways were considered based on the structural similarity of LCO with the layered material α-$NaFeO_2$, namely, the oxygen dumbbell hop (ODH) and the tetrahedral site hop (TSH),[36−38] as shown in Figure 2a−d. In the case of the ODH, Li^+ hops via a single Li vacancy. As for the TSH pathway, which requires two or more vacancies, Li^+ migrates along a curved path through a tetrahedral site.

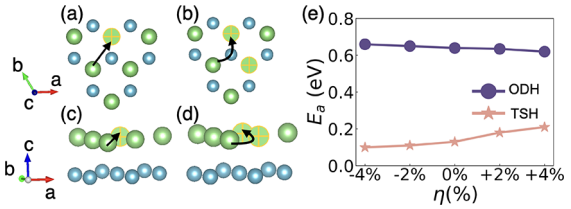

Figure 2. Left panel: (a) top view and (c) front view of the ODH diffusion path; (b) top view and (d) front view of the TSH diffusion path. Green and cyan spheres indicate Li and Co ions. Li vacancies are marked with a cross. Black arrows point in the migration direction. Only the Li^+ migration region of the system is shown for clarity. Right panel: (e) NEB migration energy barrier (E_a) results of LCO expressed as a function of biaxial strain for the ODH and TSH diffusion mechanisms, where the positive (negative) ratio corresponds to tensile (compressive) strain.

Figure 2e shows E_a results obtained as a function of the biaxial strain. It is demonstrated therein that the E_a estimated for the TSH diffusion path is always significantly lower than that of the ODH mechanism, in agreement with previous DFT results.[39] Nevertheless, E_a varies differently under biaxial strain for both mechanisms. In particular, the E_a of the ODH mechanism is reduced under increasing strain, dropping by 0.02 eV from η = 0 to +4%. In contrast, at η = +4%, the E_a of the TSH mechanism greatly increases by ∼61% compared to the value estimated at zero strain (i.e., from 0.13 to 0.21 eV). Moreover, upon compressive biaxial strain, E_a for the ODH mechanism increases slightly by 0.02 eV at η = −4%, whereas it decreases by roughly the same amount for the TSH mechanism.

Moreover, the application of uniaxial strain along the c axis yields strain along the a and b plane directions as characterized by the Poisson's ratio (∼0.24 in our calculation) of LCO. To confirm this, we proceeded to implement uniaxial strain conditions of −2 and +2%, approximating the c axis lengths corresponding to biaxial strains of −4 and +4%, respectively. Subsequently, we conducted additional NEB calculations, specifically focusing on the TSH diffusion pathway—the dominant mechanism, discussed in further detail in Section 3.2—to corroborate our supposition. The relaxed lattice parameters corresponding to these uniaxial strain conditions are outlined in Table S1b for reference. The outcomes, as depicted in Figure S3, illustrate that tensile uniaxial strain along the c axis leads to a reduction in the E_a (from 0.13 to 0.06 eV), whereas the application of compressive strain is observed to impede the diffusion process, resulting in a higher E_a (from 0.13 to 0.25 eV). This indicates that uniaxial strain might have a similar effect to biaxial strain. Acknowledging the observed similarities, our emphasis remains directed toward biaxial strain, as it has been extensively investigated in recent research concerning the strain effects induced by rapid charging in LCO.[29]

The estimated strain-induced E_a trends indicate that compressive biaxial strain could promote the overall ionic conductivity in LCO because the TSH mechanism exhibits the lowest E_a compared to that of ODH and other possible diffusion mechanisms identified in a previous study. Additionally, the TSH mechanism has been suggested to become dominating in Li^+ diffusion as the concentration of Li vacancies increases.[36,40] Nevertheless, in the zero-temperature NEB calculations, possible lattice vibrations are totally neglected, which could be very important for the ionic diffusion.[40,41] To fully test the reliability of our E_a results obtained with the zero-temperature NEB approach, FPMD simulations were conducted, as they take lattice thermal excitations into consideration without the need for assuming any particular diffusion path.[42]

3.2. Li^+ Diffusion at Finite Temperatures under Biaxial Strain. Supercells containing 183 atoms ($Li_{0.81}CoO_2$) and 177 atoms ($Li_{0.69}CoO_2$) were used in the FPMD simulations to characterize the interplay between SOC and Li^+ diffusion. Specifically, three and five Li atoms were removed from each Li plane on average, respectively. The calculated out-of-plane lattice parameter c of bulk Li_xCoO_2 (x = 0.81 and 0.69) increased to 14.19 and 14.25 Å, respectively, as compared to perfectly stoichiometric LCO (14.15 Å), whereas a showed negligible variation (Table S1a), reaching a good agreement with previous studies.[26,28,43] The highest Li vacancy concentration was fixed at 33.3% because we would like to avoid the phase transition toward a monoclinic phase.[44] The Li ordering was initialized randomly. In general, in $Li_{0.69}CoO_2$ at η = −4%, the c axis increases up to 14.60 Å (under no strain, the value is 14.25 Å), whereas at η = +4%, it is reduced to 13.94 Å. Based on the energy profiles shown in Figure S4, all of the FPMD simulations reached equilibrium after 20 ps. Therefore, the first 20 ps was disregarded in the subsequent analysis of ion diffusion.

Time-averaged mean squared displacements (MSDs) and the corresponding fit to the Arrhenius equation are shown in Figure 3a−d, and Table 1 includes the E_a values determined for each strain case. The diffusion of Li^+ is visualized via the

https://doi.org/10.1021/acsami.3c14444
ACS Appl. Mater. Interfaces 2023, 15, 53614−53622

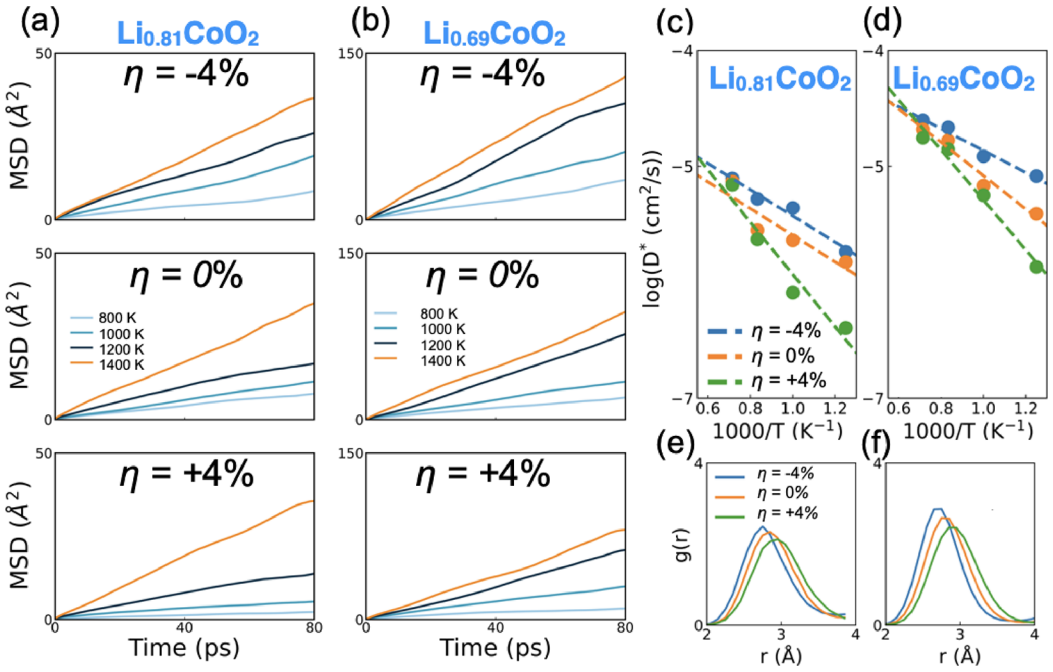

Figure 3. (a, b) Mean squared displacement calculated for Li^+ ions with FPMD simulations performed at 800, 1000, 1200, and 1400 K and considering different epitaxial strain conditions, namely, η = −4, 0, and +4% for $Li_{0.81}CoO_2$ and $Li_{0.69}CoO_2$. (c, d) Arrhenius plots of the self-diffusion coefficient in $Li_{0.81}CoO_2$ and $Li_{0.69}CoO_2$. (e, f) Radial distribution functions of Li−Li distances averaged from 20 to 100 ps in the FPMD simulations at 1200 K for η = −4, 0, and +4% for bulk $Li_{0.81}CoO_2$ and $Li_{0.69}CoO_2$.

Table 1. Activation Energy (E_a), Conductivity (σ), and Co Layer Distance Measured with FPMD Simulations for $Li_{0.81}CoO_2$ and $Li_{0.69}CoO_2$ at η = −4, 0, and +4%

	E_a (eV)	$\sigma_{300\ K}$ (S cm^{-1})	Co layer distance (Å)
$Li_{0.81}CoO_2$			
η = −4%	0.22 ± 0.02	1 × 10^{-3}	2.13
η = 0%	0.23 ± 0.05	8 × 10^{-4}	2.04
η = +4%	0.45 ± 0.06	8 × 10^{-7}	1.96
$Li_{0.69}CoO_2$			
η = −4%	0.21 ± 0.01	5 × 10^{-3}	2.10
η = 0%	0.27 ± 0.03	5 × 10^{-4}	2.00
η=+4%	0.35 ± 0.02	5 × 10^{-5}	1.91

atomic trajectories generated in the FPMD simulations (Figure S5). The barriers obtained at η = 0% with different Li vacancy concentrations are in quantitative agreement with previous analogous[37,45] first-principles and experimental studies.[37,45] The self-diffusion coefficients estimated at 300 K (Table S2), $D^*_{300\ K}$, for $Li_{0.81}CoO_2$ and $Li_{0.69}CoO_2$ are 5.3 × 10^{-9} and 4.2 × 10^{-9} cm^2/s, respectively, in good agreement with experiments.[46] Because of the high computational cost for FPMD, it was not feasible to sample a detailed range of Li contents in our study. Nevertheless, the agreement between our findings and previous work serves as a testament to the soundness of our selection and subsequent analysis.

We note that the E_a's obtained from FPMD simulations at η = 0% are slightly higher than those obtained with NEB calculations for the TSH mechanism (0.13 eV), namely, 0.23 eV for $Li_{0.81}CoO_2$ and 0.27 eV for $Li_{0.69}CoO_2$. To make them comparable, additional NEB calculations for $Li_{0.69}CoO_2$ were performed for comparison with NEB results, with E_a for the TSH diffusion pathway seeing an increasing trend for η = 0% (from 0.13 to 0.19 eV). The origins of this outcome can be understood as follows: (1) the TSH mechanism is the dominant one in the presence of vacancies,[36] and (2) the effective positive charge of the Co ions increases when the concentration of Li vacancies increases, thus electrostatically hindering Li^+ diffusion.[37] Table 1 also shows that the E_a estimated for $Li_{0.81}CoO_2$ at η = −4% (0.22 eV) is close to the η = 0% value (0.23 eV), whereas under biaxial tensile strain, it is doubled (0.45 eV). It is noteworthy that in the case of $Li_{0.81}CoO_2$, compressive strain does not have a significant effect on E_a. (The corresponding ionic conductivity, σ, was found to increase slightly with respect to the zero-strain case, although the small increment can be ascribed to a fitting error.) Meanwhile, when the Li deficiency is further increased, the compressive strain clearly enhances the Li^+ diffusion. In particular, E_a decreases by 0.06 eV for η = −4% in comparison to the zero-strain case. Likewise, the accompanying ionic conductivities increase by 1 and 2 orders of magnitude (Table 1). The additional NEB calculations for $Li_{0.69}CoO_2$ also confirm this trend (0.17 eV for η = −4% and 0.19 eV for η = 0%), whereas the reverse is true for tensile strain.

To gain insight into the variations in the Li^+ migration properties, we conducted an analysis of the local structure parameters. First, we performed a comparison of the Li layer distances and Co layer distances (shown in Figure S6) under η = −4, 0, and +4%. A linear correlation between the Co layer distance and E_a can be observed, as shown in Table 1. For example, the Co layer distance is reduced by approximately 4% under η = +4%, resulting in an E_a increase of nearly 100 and 30% for $Li_{0.81}CoO_2$ and $Li_{0.69}CoO_2$, respectively. On the other hand, η = −4% results in a larger Co layer distance and consequently leads to a lower E_a, especially in $Li_{0.69}CoO_2$ (a layer expansion of approximately 6% leads to an E_a reduction of 20%). Notably, a larger Co layer distance results in smaller electrostatic repulsive interactions during Li^+ migration along the TSH pathway, which could promote Li^+ diffusion.[36,47] Furthermore, Li layer distances (Table S3) also show a trivial

https://doi.org/10.1021/acsami.3c14444
ACS Appl. Mater. Interfaces 2023, 15, 53614−53622

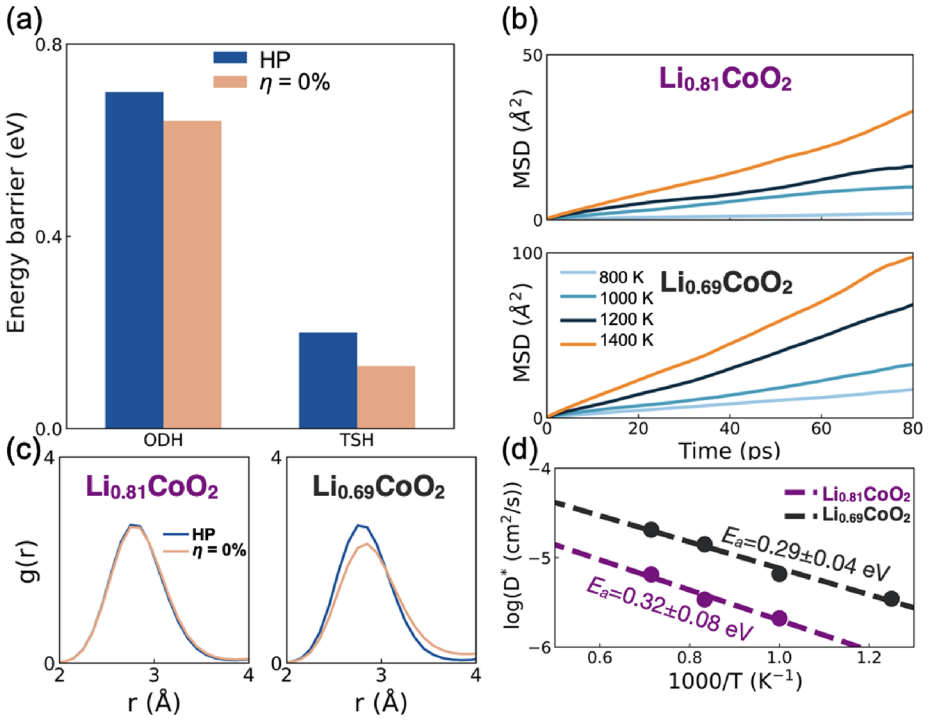

Figure 4. (a) Calculated DFT-NEB energy barrier (E_a) for Li^+ diffusion along two different pathways (ODH and TSH) for LCO under hydrostatic pressure (HP) and strain-free cases. (b) Mean square displacement (MSD) calculated for Li^+ ions from FPMD simulations performed at 800, 1000, 1200, and 1400 K under an HP of 1 GPa in $Li_{0.81}CoO_2$ and $Li_{0.69}CoO_2$. During the first 20 ps of the FPMD simulations, the system was equilibrated; hence, this interval of time was excluded from our analysis. (c) Radial distribution functions (RDFs) of Li−Li distances averaged from 20 to 100 ps in the FPMD simulation at 1200 K for η = 0% and HP in bulk $Li_{0.81}CoO_2$ and $Li_{0.69}CoO_2$. (d) Arrhenius plots of the Li^+ self-diffusion coefficients in $Li_{0.81}CoO_2$ and $Li_{0.69}CoO_2$ under 1 GPa HP.

increase under compressive strain, which could also provide additional room for Li^+ diffusion through the TSH mechanism, leading to lower E_a. Additionally, we analyzed the Li−Li radial distribution functions (RDFs), as depicted in Figure 3e,f. As the *a* and *b* axes were compressed or enlarged, the peaks of the RDFs shifted toward the left or right, along with increased or decreased maximum populations of Li−Li distances, which were consistent with the η = −4 and +4% conditions, respectively. In the compressive situation, the Li−Li distances thus decrease, which increase Coulomb repulsion and destabilize the Li at its site, consequently resulting in a lower energy barrier. Such a shortened Li−Li distance could promote Li^+ diffusion and conduction.

The Li^+ diffusion enhancement effect observed under compressive biaxial strain strongly depends on the Li vacancy concentration.[48] As previously mentioned, the E_a and $\sigma_{300\ K}$ calculated for $Li_{0.81}CoO_2$ at η = −4% do not appreciably vary from the values obtained at zero strain (see, e.g., the Li^+ trajectory densities in Figure S5). The specific vacancy concentration at which the Li^+ diffusion enhancement effect occurs under compressive biaxial strain is currently unknown and requires further investigation. Nevertheless, it is still plausible that compressive strain can promote the Li^+ diffusion via creating Li/Co layer distance variation and increasing the Li−Li Coulomb repulsion. Previous studies have reported such cases of increased diffusivity with similar mechanisms due to compressive strain for various materials.[49−51]

3.3. Li^+ Diffusion under Hydrostatic Pressure (HP). We also investigated Li^+ diffusion under 1 GPa of HP in LCO, as such a scenario occurs during the packaging of batteries and in different performance and safety tests.[52] NEB calculations show that upon 1 GPa of hydrostatic pressure, the activation energy for Li^+ diffusion of both the ODH and TSH pathways increases by 0.02 eV (Figure 4a).

To further investigate the Li^+ migration behavior, FPMD simulations were also performed to mix all the diffusion pathways and take lattice thermal excitations into consideration. Figure 4b shows the MSD results obtained for $Li_{0.81}CoO_2$ and $Li_{0.69}CoO_2$ in our FPMD simulations. Note that we disregard the case of 800 K for $Li_{0.81}CoO_2$, when fitting $D(T)$ to the Arrhenius equation due to the negligible MSD (average MSD per atom of less than 3 $Å^2$ over 80 ps). E_a for Li^+ migration rises from 0.23 (Table 1) to 0.32 eV in $Li_{0.81}CoO_2$, but it decreases to 0.29 eV in $Li_{0.69}CoO_2$ (Figure 4d).

Analysis of the local structure parameters was performed to understand the diffusion-suppressing effect of HP. Table S4 indicates that under HP, the *c* lattice parameters of $Li_{0.81}CoO_2$ and $Li_{0.69}CoO_2$ decrease by 0.06 and 0.08 Å, respectively, compared to the unstressed system (Table S1a). Table S5 shows that only the Li layer distance undergoes a minor contraction, whereas the Co layer distance remains relatively unchanged. This leads to an increase in E_a for Li^+ migration. However, our observations also reveal that the *a* and *b* lattice parameters of $Li_{0.81}CoO_2$ and $Li_{0.69}CoO_2$ decrease by 0.3 and 0.5%, respectively. Combined with RDF analysis (refer to Figure 4c), we find that the Li−Li peak shifts to the left, indicating a shortened Li−Li distance when the Li vacancy concentration increases in $Li_{0.69}CoO_2$ (this effect is not seen for $Li_{0.81}CoO_2$). This indicates a stronger Coulomb repulsion, which could offset the negative effect of smaller Li layer distances and promote Li^+ diffusion, thus explaining why E_a

https://doi.org/10.1021/acsami.3c14444
ACS Appl. Mater. Interfaces 2023, 15, 53614−53622

drops in $Li_{0.69}CoO_2$. Although the activation energy in $Li_{0.69}CoO_2$ is lower than that of $Li_{0.81}CoO_2$, it is still higher than that of the unstressed system (0.27 eV, Table 1), suggesting that the application of HP could lead to a decrease in Li^+ diffusion in $LiCoO_2$.

Similar to E_a, which characterizes the Li ionic diffusivity through an Arrhenius-type relation (eq 2), a characteristic activation volume (V_a) for conduction can describe the pressure-dependent evolution of ionic conductivity.[53] V_a and E_a are interconnected, with V_a capturing the changes in E_a as stress is applied. Given the influence of Co and Li layer distance variations, it is also important to consider the role of V_a in the migration process, which provides additional insights into the migration mechanism and the interplay between the material structure and the migration pathway.[54] We performed additional NEB calculations of LCO to obtain the E_a under 2, 3, 4, and 5 GPa of HP. V_a is obtained as follows:[55]

$$V_a = \left[\frac{\partial E_a}{\partial p}\right]_T \tag{5}$$

where p is the pressure and T is the temperature. The V_a for LCO under hydrostatic pressure is obtained as 2.6 ± 0.1 cm^3/mol. Note that we only considered the TSH diffusion pathway as it is the dominant one in LCO under the presence of vacancies (see Sec 3.2). The V_a can be further extended in tensor form utilizing the conventional concept of the elastic stiffness tensor in the elastic theory, as follows:

$$V_{aij} = \left[\frac{\partial E_a}{\partial \sigma_{ij}}\right]_T = \left[C^{-1}_{ijkl}\frac{\partial E_a}{\partial \varepsilon_{ij}}\right]_T = \begin{bmatrix} 2.85 & 0 & 0 \\ 0 & 2.85 & 0 \\ 0 & 0 & 2.28 \end{bmatrix} \tag{6}$$

where C_{ijkl} is the elastic stiffness tensor of LCO, σ_{ij} the stress tensor, and ε_{ij} the strain tensor under HP.

We refer to Supporting Discussion 2 for a more detailed derivation of Equation 6. To the best of our knowledge, it is the first time that the V_a and its tensor form of LCO are reported. A nonzero activation volume serves as an indicator of a disparity between the available free volume within the structure and the volume necessary for efficient ion migration. A positive V_a shows that Li^+ ions need to open up the space for diffusion, as described in previous studies for $Li_{10}GeP_2S_{12}$ (+2.17 cm^3/mol),[55] Na_3PS_4 (+1.78 cm^3/mol for high temperature),[54] and t-Li_7SiPS_8 (+1.7−2.0 cm^3/mol).[56] On the other hand, a negative V_a, indicating an enhanced ionic diffusivity under increasing pressure, is also observed in certain cases, for example, Ag_3SI (−2.3 ± 0.4 cm^3/mol) and Li-β-Al_2O_3 (−0.7 cm^3/mol).[57] Our V_a shows consistent results with our AIMD calculation, i.e., that Li^+ diffusion decreases under external HP, given the shrinkage of the diffusion space. Inspired by the work carried out by Jagad et al.,[58] we explored a two-step fitting by adding HP and V_a into the Arrhenius equation. Comparing one-step and two-step fitting (Figure S8), E_a for $Li_{0.81}CoO_2$ increased slightly from 0.32 to 0.34 eV, whereas E_a for $Li_{0.69}CoO_2$ does not show a significant change between two fitting procedures. Moreover, D_0 of $Li_{0.81}CoO_2$ decreases from 3×10^{-10} to 1.8×10^{-10} cm^2/s, whereas that of $Li_{0.81}CoO_2$ remains relatively constant. Despite these minor effects, our conclusion on the tuned Li^+ diffusion under HP in LCO remains unchanged. For consistency with biaxial strain effects, we thus retained the one-step fitting results.

3.4. Li Vacancy Formation Energy under Biaxial Strain and HP. The formation energy (E_V) of a Li vacancy (V_{Li}) is a critical quantity in the evaluation of Li^+ transport because V_{Li} affects the intercalation potential and rate capability of cathode materials. Note that the calculated E_V is given with respect to the Li metal (see Section 2). The effects of biaxial strain and HP on E_V were estimated for $LiCoO_2$. As shown in Figure 5, the average E_V calculated for $LiCoO_2$

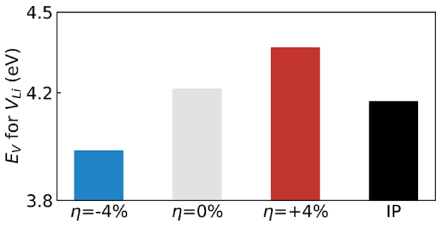

Figure 5. Formation energy (E_V) of a single Li vacancy for $LiCoO_2$ under η = −4, 0, and +4% and HP.

amounts to 4.21 eV at η = 0%, which is in good agreement with previous DFT studies.[8,59,60] E_V for $LiCoO_2$ is reduced by 0.2 eV under η = −4% and increased by 0.15 eV under η = +4% with respect to the η = 0% case. We expressed E_V as a function of biaxial strain and obtained the xx (or yy) component of the elastic dipole tensor (both 4.74 eV) with respect to the biaxial strain,[61,62] as shown in Figure S9. Moreover, the variation of E_V suggests that compressive strain makes it easier to remove Li^+ from the cathode material, which leads to a lower intercalation potential. Regarding the application of HP, we found that the average E_V of LCO is 0.05 eV lower than that of the analogous uncompressed system. Bader charge analysis (Table S7) shows that under compressive biaxial strain, the Li^+ ions concede on average less charge to the nearby O ions than under tensile strain, thus indicating weaker bonding interactions. A weaker interaction results in a lower E_V and easier Li^+ extraction. Lastly, the nearest average Li−Li distances under different strain cases were evaluated. In the compressive case (η = −4%), the average distance is reduced by 0.07 Å, indicating a stronger Li−Li Coulomb repulsion interaction, which also contributes to a lower E_V. Meanwhile, in the tensile case (η = +4%), the distance is increased by 0.11 Å, correspondingly resulting in a higher E_V. A lower E_V can limit the performance of energy storage devices by reducing the intercalation voltage and, ultimately, the energy density of the cathode material.

4. CONCLUSIONS

We have presented a comprehensive first-principles study of the Li^+ diffusion properties of SOC LCO under biaxial strain and an HP of around 1 GPa. By performing both NEB and FPMD calculations, we found that compressive biaxial strain tends to enhance Li^+ diffusivity, whereas tensile biaxial strain suppresses it. FPMD simulations show that compressive strain does not tend to promote Li^+ diffusion when Li deficiencies are low, whereas tensile biaxial strain always tends to hinder the diffusion. Our results demonstrated that, under compressive strain, the Co layer distance was greatly increased, leading to an easier diffusion of Li^+ along the TSH pathway by reducing the activation energy. Moreover, a stronger Coulomb interaction between Li-ions also contributed to Li^+ diffusion. In contrast, HP could decrease Li^+ diffusion in LCO, primarily by reducing the Li layer distance, with Coulomb repulsion

https://doi.org/10.1021/acsami.3c14444
ACS Appl. Mater. Interfaces 2023, 15, 53614−53622

between Li-ions partially offsetting this effect. However, the resulting increase in E_a of Li^+ migration ultimately results in a decrease in Li^+ diffusion. The results thus highlight the interplay among mechanical strain, variations in Li/Co layer distance, Li−Li distance, state-of-charge, and Li^+ diffusion in LCO. A V_a ~2.6 ± 0.1 cm^3/mol for LCO under HP is reported for the first time, indicating that Li migration requires additional space. Moreover, the calculated formation energies of a single Li vacancy show that Li vacancies are more likely to be created under compressive biaxial strain than under tensile strain, which could subsequently lead to a lower energy density. This trend is due to a weaker Li−O interaction, as demonstrated by the Bader charge analysis and supported by a strong Li−Li Coulomb interaction. Meanwhile, HP has a relatively minor effect on the formation of a single Li vacancy. The present results provide guidance on LCO cathode control, in which the strain effect should be taken into account, and can be generalized to other layered oxide cathodes to stimulate research efforts in this direction.

■ ASSOCIATED CONTENT

Supporting Information

The Supporting Information is available free of charge at https://pubs.acs.org/doi/10.1021/acsami.3c14444.

Stress tensor components for LCO as a function of the biaxial strain and hydrostatic pressure; strain along the *a* and *c* axes for LCO as a function of biaxial strain; NEB migration energy barrier for TSH pathway in LCO as a function of uniaxial strain; energy evolutions and corresponding energies averaged in FPMD; Li^+ trajectory of FPMD; lattice parameter, layer distance, and diffusion coefficient for LCO under different concentrations, strains, and hydrostatic pressures; band gap and effective mass for LCO under biaxial strain and hydrostatic pressure; (Supporting Discussion 1) electronic conductivity of LCO under biaxial strain and hydrostatic pressure; and (Supporting Discussion 2) activation volume defined in tensor form (PDF)

■ AUTHOR INFORMATION

Corresponding Authors

Zizhen Zhou − *Graduate School of Advanced Science and Engineering, Waseda University, Tokyo 169-8555, Japan; Research Center for Energy and Environmental Materials (GREEN), National Institute for Materials Science (NIMS), Ibaraki 305-0044, Japan*; Email: zizhen_zhou@toki.waseda.jp

Yoshitaka Tateyama − *Graduate School of Advanced Science and Engineering, Waseda University, Tokyo 169-8555, Japan; Research Center for Energy and Environmental Materials (GREEN), National Institute for Materials Science (NIMS), Ibaraki 305-0044, Japan; Laboratory for Chemistry and Life Science, Tokyo Institute of Technology, Yokohama 226-8503, Japan*; orcid.org/0000-0002-5532-6134; Email: tateyama.yoshitaka@nims.go.jp

Authors

Claudio Cazorla − *Departament de Física, Universitat Politècnica de Catalunya, E-08034 Barcelona, Spain*; orcid.org/0000-0002-6501-4513

Bo Gao − *Research Center for Energy and Environmental Materials (GREEN), National Institute for Materials Science (NIMS), Ibaraki 305-0044, Japan; College of Materials Science and Engineering, Jilin University, Changchun, Jilin 130012, People's Republic of China*

Huu Duc Luong − *Research Center for Energy and Environmental Materials (GREEN), National Institute for Materials Science (NIMS), Ibaraki 305-0044, Japan*

Toshiyuki Momma − *Graduate School of Advanced Science and Engineering, Waseda University, Tokyo 169-8555, Japan*

Complete contact information is available at: https://pubs.acs.org/10.1021/acsami.3c14444

Author Contributions

Z.Z. and Y.T. conceived the study with the help of C.C., B.G., L.D., and T.M. Calculations were performed by Z.Z. Contributions were made by Y.T., C.C., B.G., L.D., and T.M. in relation to the analysis and discussion of the results. The manuscript was written by Z.Z. with input/comments/feedback from other authors.

Notes

The authors declare no competing financial interest.

■ ACKNOWLEDGMENTS

This work was supported in part by JSPS KAKENHI grant JP19H05815, MEXT as "Program for Promoting Research on the Supercomputer Fugaku" grants JPMXP1020200301 and JPMXP1020230325, Data Creation and Utilization Type Material Research and Development Project grant JPMXP1121467561, as well as JST COI-NEXT grant JPMJPF2016. The calculations were performed on the supercomputers at NIMS (Numerical Materials Simulator) and the supercomputer Fugaku at the RIKEN through the HPCI System Research Project (project IDs: hp220059 and hp220177). Z.Z. would like to thank Ane Eline Herlyng for proofreading

■ REFERENCES

(1) Qin, Z.; Zhang, Y.; Luo, W.; Zhang, T.; Wang, T.; Ni, L.; Wang, H.; Zhang, N.; Liu, X.; Zhou, J.; Chen, G. A Universal Molten Salt Method for Direct Upcycling of Spent Ni-Rich Cathode towards Single-Crystalline Li-Rich Cathode. *Angew. Chem., Int. Ed.* **2023**, *62* (25), No. e202218672.

(2) Ugata, Y.; Yukishita, K.; Kazahaya, N.; Takahashi, S.; Yabuuchi, N. Nonflammable Fluorinated Ester-Based Electrolytes for Safe and High-Energy Batteries with $LiCoO_2$. *Chem. Mater.* **2023**, *35* (9), 3686−3693.

(3) Goodenough, J. B.; Kim, Y. Challenges for Rechargeable Li Batteries. *Chem. Mater.* **2010**, *22* (3), 587−603.

(4) Fergus, J. W. Recent Developments in Cathode Materials for Lithium Ion Batteries. *J. Power Sources* **2010**, *195* (4), 939−954.

(5) Zhou, J.; Notten, P. H. L. Studies on the Degradation of Li-Ion Batteries by the Use of Microreference Electrodes. *J. Power Sources* **2008**, *177* (2), 553−560.

(6) Tan, Z.; Li, Y.; Xi, X.; Jiang, S.; Li, X.; Shen, X.; Zhang, P.; He, Z.; Zheng, J. A Novelty Strategy Induced Pinning Effect and Defect Structure in Ni-Rich Layered Cathodes towards Boosting Its Electrochemical Performance. *Journal of Energy Chemistry* **2022**, *72*, 570−580.

(7) Tokranov, A.; Sheldon, B. W.; Lu, P.; Xiao, X.; Mukhopadhyay, A. The Origin of Stress in the Solid Electrolyte Interphase on Carbon Electrodes for Li Ion Batteries. *J. Electrochem. Soc.* **2014**, *161* (1), A58.

(8) Gao, B.; Jalem, R.; Ma, Y.; Tateyama, Y. Li^+ Transport Mechanism at the Heterogeneous Cathode/Solid Electrolyte Interface in an All-Solid-State Battery via the First-Principles Structure Prediction Scheme. *Chem. Mater.* **2020**, *32* (1), 85−96.

(9) Mukhopadhyay, A.; Tokranov, A.; Xiao, X.; Sheldon, B. W. Stress Development Due to Surface Processes in Graphite Electrodes for Li-Ion Batteries: A First Report. *Electrochim. Acta* **2012**, *66*, 28−37.
(10) Hao, F.; Fang, D. Diffusion-Induced Stresses of Spherical Core-Shell Electrodes in Lithium-Ion Batteries: The Effects of the Shell and Surface/Interface Stress. *J. Electrochem. Soc.* **2013**, *160* (4), A595.
(11) Suthar, B.; Northrop, P. W. C.; Braatz, R. D.; Subramanian, V. R. Optimal Charging Profiles with Minimal Intercalation-Induced Stresses for Lithium-Ion Batteries Using Reformulated Pseudo 2-Dimensional Models. *J. Electrochem. Soc.* **2014**, *161* (11), F3144.
(12) Ngandjong, A. C.; Lombardo, T.; Primo, E. N.; Chouchane, M.; Shodiev, A.; Arcelus, O.; Franco, A. A. Investigating Electrode Calendering and Its Impact on Electrochemical Performance by Means of a New Discrete Element Method Model: Towards a Digital Twin of Li-Ion Battery Manufacturing. *J. Power Sources* **2021**, *485*, No. 229320.
(13) Lim, H. D.; Park, J. H.; Shin, H. J.; Jeong, J.; Kim, J. T.; Nam, K. W.; Jung, H. G.; Chung, K. Y. A Review of Challenges and Issues Concerning Interfaces for All-Solid-State Batteries. *Energy Storage Materials.* **2020**, *25*, 224−250.
(14) Hao, F.; Chen, X. First-Principles Study of Lithium Adsorption and Diffusion on Graphene: The Effects of Strain. *Mater. Res. Express* **2015**, *2* (10), No. 105016.
(15) Zhang, Q.; Tang, C.; Zhu, W.; Cheng, C. Strain-Enhanced Li Storage and Diffusion on the Graphyne as the Anode Material in the Li-Ion Battery. *J. Phys. Chem. C* **2018**, *122* (40), 22838−22848.
(16) Lee, J.; Pennycook, S. J.; Pantelides, S. T. Simultaneous Enhancement of Electronic and Li^+ Ion Conductivity in $LiFePO_4$. *Appl. Phys. Lett.* **2012**, *101* (3), No. 033901.
(17) Tealdi, C.; Heath, J.; Islam, M. S. Feeling the Strain: Enhancing Ionic Transport in Olivine Phosphate Cathodes for Li- and Na-Ion Batteries through Strain Effects. *J. Mater. Chem. A* **2016**, *4* (18), 6998−7004.
(18) Cheng, Y.-T.; Verbrugge, M. W. Diffusion-Induced Stress, Interfacial Charge Transfer, and Criteria for Avoiding Crack Initiation of Electrode Particles. *J. Electrochem. Soc.* **2010**, *157* (4), A508.
(19) Lyu, Y.; Wu, X.; Wang, K.; Feng, Z.; Cheng, T.; Liu, Y.; Wang, M.; Chen, R.; Xu, L.; Zhou, J. An Overview on the Advances of $LiCoO_2$ Cathodes for Lithium-Ion Batteries. *Adv. Energy Mater.* **2021**, *11* (2), No. 2000982.
(20) Diercks, D. R.; Musselman, M.; Morgenstern, A.; Wilson, T.; Kumar, M.; Smith, K.; Kawase, M.; Gorman, B. P.; Eberhart, M.; Packard, C. E. Evidence for Anisotropic Mechanical Behavior and Nanoscale Chemical Heterogeneity in Cycled $LiCoO_2$. *J. Electrochem. Soc.* **2014**, *161* (11), F3039−F3045.
(21) Mukhopadhyay, A.; Sheldon, B. W. Deformation and Stress in Electrode Materials for Li-Ion Batteries. *Prog. Mater. Sci.* **2014**, *63*, 58−116.
(22) Choi, Y.-M.; Pyun, S.-I. Effects of Intercalation-Induced Stress on Lithium Transport through Porous $LiCoO_2$ Electrode. *Solid State Ionics* **1997**, *99* (3−4), 173−183.
(23) Kresse, G.; Furthmüller, J. Efficient Iterative Schemes for *Ab Initio* Total-Energy Calculations Using a Plane-Wave Basis Set. *Phys. Rev. B* **1996**, *54* (16), 11169−11186.
(24) Blöchl, P. E. Projector Augmented-Wave Method. *Phys. Rev. B* **1994**, *50* (24), 17953−17979.
(25) Zhou, F.; Cococcioni, M.; Marianetti, C. A.; Morgan, D.; Ceder, G. First-Principles Prediction of Redox Potentials in Transition-Metal Compounds with LDA + U. *Phys. Rev. B* **2004**, *70* (23), No. 235121.
(26) Laubach, S.; Laubach, S.; Schmidt, P. C.; Ensling, D.; Schmid, S.; Jaegermann, W.; Thißen, A.; Nikolowski, K.; Ehrenberg, H. Changes in the Crystal and Electronic Structure of $LiCoO_2$ and $LiNiO_2$ upon Li Intercalation and de-Intercalation. *Phys. Chem. Chem. Phys.* **2009**, *11* (17), 3278−3289.
(27) Wu, L.; Zhang, J. *Ab Initio* Study of Anisotropic Mechanical Properties of $LiCoO_2$ during Lithium Intercalation and Deintercalation Process. *J. Appl. Phys.* **2015**, *118* (22), No. 225101.
(28) Kramer, D.; Ceder, G. Tailoring the Morphology of $LiCoO_2$: A First Principles Study. *Chem. Mater.* **2009**, *21* (16), 3799−3809.
(29) Zhu, Y.; Wu, D.; Yang, X.; Zeng, L.; Zhang, J.; Chen, D.; Wang, B.; Gu, M. Microscopic Investigation of Crack and Strain of $LiCoO_2$ Cathode Cycled under High Voltage. *Energy Storage Mater.* **2023**, *60*, No. 102828.
(30) Wang, L.; Li, B.; Chen, J.; Li, J.; Luo, Y.; Lv, T. Coupled Effect of SOC and SOH on Tensile Behaviors of Lithium-Ion Battery Electrodes. *J. Energy Storage* **2023**, *68*, No. 107782.
(31) Tealdi, C.; Mustarelli, P. Improving Oxygen Transport in Perovskite-Type $LaGaO_3$ Solid Electrolyte through Strain. *J. Phys. Chem. C* **2014**, *118* (51), 29574−29582.
(32) Henkelman, G.; Uberuaga, B. P.; Jónsson, H. A Climbing Image Nudged Elastic Band Method for Finding Saddle Points and Minimum Energy Paths. *J. Chem. Phys.* **2000**, *113* (22), 9901−9904.
(33) Momma, K.; Izumi, F. VESTA 3 for Three-Dimensional Visualization of Crystal, Volumetric and Morphology Data. *J. Appl. Crystallogr.* **2011**, *44* (6), 1272−1276.
(34) Deng, Z.; Zhu, Z.; Chu, I. H.; Ong, S. P. Data-Driven First-Principles Methods for the Study and Design of Alkali Superionic Conductors. *Chem. Mater.* **2017**, *29* (1), 281−288.
(35) He, X.; Zhu, Y.; Epstein, A.; Mo, Y. Statistical Variances of Diffusional Properties from *Ab Initio* Molecular Dynamics Simulations. *npj Comput. Mater.* **2018**, *4* (1), 18.
(36) Van der Ven, A.; Ceder, G. Lithium Diffusion Mechanisms in Layered Intercalation Compounds. *J. Power Sources* **2001**, *97*−*98*, 529−531.
(37) Van der Ven, A.; Ceder, G. Lithium Diffusion in Layered Li_xCoO_2. *Electrochem. Solid-State Lett.* **2000**, *3* (7), 301.
(38) Liu, X.; Shi, J.; Zheng, B.; Chen, Z.; Su, Y.; Zhang, M.; Xie, C.; Su, M.; Yang, Y. Constructing a High-Energy and Durable Single-Crystal NCM811 Cathode for All-Solid-State Batteries by a Surface Engineering Strategy. *ACS Appl. Mater. Interfaces* **2021**, *13* (35), 41669−41679.
(39) Kang, K.; Ceder, G. Factors That Affect Li Mobility in Layered Lithium Transition Metal Oxides. *Phys. Rev. B* **2006**, *74* (9), No. 094105.
(40) Li, J.-J.; Dai, Y.; Zheng, J.-C. Strain Engineering of Ion Migration in $LiCoO_2$. *Front. Phys.* **2022**, *17* (1), 13503.
(41) Ning, F.; Li, S.; Xu, B.; Ouyang, C. Strain Tuned Li Diffusion in $LiCoO_2$ Material for Li Ion Batteries: A First Principles Study. *Solid State Ion* **2014**, *263*, 46−48.
(42) Sagotra, A. K.; Chu, D.; Cazorla, C. Influence of Lattice Dynamics on Lithium-Ion Conductivity: A First-Principles Study. *Phys. Rev. Mater.* **2019**, *3* (3), No. 035405.
(43) Yaqoob, N.; Mücke, R.; Guillon, O.; Kaghazchi, P. Delithiation-Induced Oxygen Vacancy Formation Increases Microcracking of $LiCoO_2$ Cathodes. *J. Power Sources* **2022**, *533*, No. 231316.
(44) Chen, Z.; Dahn, J. R. Methods to Obtain Excellent Capacity Retention in $LiCoO_2$ Cycled to 4.5 V. *Electrochim. Acta* **2004**, *49* (7), 1079−1090.
(45) Nakamura, K.; Ohno, H.; Okamura, K.; Michihiro, Y.; Moriga, T.; Nakabayashi, I.; Kanashiro, T. ^7Li NMR Study on Li^+ Ionic Diffusion and Phase Transition in Li_xCoO_2. *Solid State Ion* **2006**, *177* (9−10), 821−826.
(46) Sugiyama, J.; Mukai, K.; Ikedo, Y.; Nozaki, H.; Månsson, M.; Watanabe, I. Li Diffusion in Li_xCoO_2 Probed by Muon-Spin Spectroscopy. *Phys. Rev. Lett.* **2009**, *103* (14), No. 147601.
(47) Kang, K.; Meng, Y. S.; Bréger, J.; Grey, C. P.; Ceder, G. Electrodes with High Power and High Capacity for Rechargeable Lithium Batteries. *Science (1979)* **2006**, *311* (5763), 977−980.
(48) Qi, Y.; Hector, L. G.; James, C.; Kim, K. J. Lithium Concentration Dependent Elastic Properties of Battery Electrode Materials from First Principles Calculations. *J. Electrochem. Soc.* **2014**, *161* (11), F3010.
(49) Zou, Z.; Ma, N.; Wang, A.; Ran, Y.; Song, T.; Jiao, Y.; Liu, J.; Zhou, H.; Shi, W.; He, B.; Wang, D.; Li, Y.; Avdeev, M.; Shi, S. Relationships Between Na+ Distribution, Concerted Migration, and

Diffusion Properties in Rhombohedral NASICON. *Adv. Energy Mater.* **2020**, *10* (30), No. 2001486.
(50) Kozinsky, B.; Akhade, S. A.; Hirel, P.; Hashibon, A.; Elsässer, C.; Mehta, P.; Logeat, A.; Eisele, U. Effects of Sublattice Symmetry and Frustration on Ionic Transport in Garnet Solid Electrolytes. *Phys. Rev. Lett.* **2016**, *116* (5), No. 055901.
(51) Düvel, A.; Heitjans, P.; Fedorov, P.; Scholz, G.; Cibin, G.; Chadwick, A. V.; Pickup, D. M.; Ramos, S.; Sayle, L. W. L.; Sayle, E. K. L.; Sayle, T. X. T.; Sayle, D. C. Is Geometric Frustration-Induced Disorder a Recipe for High Ionic Conductivity? *J. Am. Chem. Soc.* **2017**, *139* (16), 5842−5848.
(52) Barai, A.; Guo, Y.; McGordon, A.; Jennings, P. A Study of the Effects of External Pressure on the Electrical Performance of a Lithium-Ion Pouch Cell. *2013 Int. Conf. Connected Vehicles Expo (ICCVE)* **2013**, 295−299.
(53) Hoshino, H.; Yanagiya, H.; Shimoji, M. Effect of Hydrostatic Pressure on the Electrical Conductivity of Ag_3SBr and β-Ag_3SI. *Journal of the Chemical Society, Faraday Transactions 1: Physical Chemistry in Condensed Phases* **1974**, *70*, 281−286.
(54) Famprikis, T.; Kudu, O. U.; Dawson, J. A.; Canepa, P.; Fauth, F.; Suard, E.; Zbiri, M.; Dambournet, D.; Borkiewicz, O. J.; Bouyanfif, H.; Emge, S. P.; Cretu, S.; Chotard, J. N.; Grey, C. P.; Zeier, W. G.; Islam, M. S.; Masquelier, C. Under Pressure: Mechanochemical Effects on Structure and Ion Conduction in the Sodium-Ion Solid Electrolyte Na_3PS_4. *J. Am. Chem. Soc.* **2020**, *142* (43), 18422−18436.
(55) Fu, Z. H.; Chen, X.; Zhao, C. Z.; Yuan, H.; Zhang, R.; Shen, X.; Ma, X. X.; Lu, Y.; Liu, Q. B.; Fan, L. Z.; Zhang, Q. Stress Regulation on Atomic Bonding and Ionic Diffusivity: Mechanochemical Effects in Sulfide Solid Electrolytes. *Energy Fuels* **2021**, *35* (12), 10210−10218.
(56) Schneider, C.; Schmidt, C. P.; Neumann, A.; Clausnitzer, M.; Sadowski, M.; Harm, S.; Meier, C.; Danner, T.; Albe, K.; Latz, A.; Wall, W. A.; Lotsch, B. V. Effect of Particle Size and Pressure on the Transport Properties of the Fast Ion Conductor *t*-Li_7SiPS_8. *Adv. Energy Mater.* **2023**, *13* (15), No. 2203873.
(57) Radzilowski, R. H.; Kummer, J. T. The Hydrostatic Pressure Dependence of the Ionic Conductivity of β-Aluminas. *J. Electrochem. Soc.* **1971**, *118* (5), 714.
(58) Jagad, H. D.; Harris, S. J.; Sheldon, B. W.; Qi, Y. Tradeoff between the Ion Exchange-Induced Residual Stress and Ion Transport in Solid Electrolytes. *Chem. Mater.* **2022**, *34* (19), 8694−8704.
(59) Haruyama, J.; Sodeyama, K.; Han, L.; Takada, K.; Tateyama, Y. Space−Charge Layer Effect at Interface between Oxide Cathode and Sulfide Electrolyte in All-Solid-State Lithium-Ion Battery. *Chem. Mater.* **2014**, *26* (14), 4248−4255.
(60) Hoang, K.; Johannes, M. D. Defect Chemistry in Layered Transition-Metal Oxides from Screened Hybrid Density Functional Calculations. *J. Mater. Chem. A Mater.* **2014**, *2* (15), 5224−5235.
(61) James, C.; Wu, Y.; Sheldon, B.; Qi, Y. Computational Analysis of Coupled Anisotropic Chemical Expansion in $Li_{2-X}MnO_{3-\delta}$. *MRS Adv.* **2016**, *1* (15), 1037−1042.
(62) Gillan, M. J. The Elastic Dipole Tensor for Point Defects in Ionic Crystals. *Journal of Physics C: Solid State Physics* **1984**, *17* (9), 1473.

https://doi.org/10.1021/acsami.3c14444
ACS Appl. Mater. Interfaces 2023, 15, 53614−53622